EngOpt 2012 - International Conference on Engineering Optimization
Rio de Janeiro, Brazil, 1-5 July 2012.

Simultaneous estimation of experimental and material parameters

G. J. Jansen van Rensburg[1], S. Kok[2], D. N. Wilke[3]

[1,2] Modelling and Digital Science, Council for Scientific and Industrial Research, Pretoria, South Africa.
[1,3] Department of Mechanical and Aeronautical Engineering, University of Pretoria, Pretoria, South Africa.
[1]jjvrensburg@csir.co.za, [2]skok@csir.co.za, [3]nico.wilke@up.ac.za

Abstract

This conference contribution focusses on the invertibility of non-ideal material tests to accurately determine material parameters. This is done by attempting to model non-ideal test cases and comparing strains as well as force history to the experimental data. An inverse analysis is performed that determines material properties and boundary conditions simultaneously.

This idea is investigated using virtual experimental data. The virtual experimental data is obtained by performing a finite element analysis with known material parameters and boundary conditions. The inverse analysis then aims to recover the known material and boundary conditions without using any prior knowledge of the true parameters. This is done to see if such a problem is in fact invertible and if the material and test parameters can be estimated simultaneously.

Keywords: Inverse analysis, Parameter identification, Material model calibration

1 Introduction

Material testing usually makes use of a simple geometry subjected to a simple load case. The goal is to obtain uniform stress states so that simple analytical post processing would produce stress-strain curves. Specific standards and procedures are in place for these tests. If a compression test is performed under ideal conditions, experimental data can be used to calibrate a material model with little effort.

However, in the case of hard material compression testing, the high stiffness of the specimen compared to the effective stiffness of the test machine can result in a non-ideal material test. For this work, experimental data (hydraulic cylinder displacement, load cell and strain gauges) for a number of compression tests are available at different temperatures. This data demonstrates that a non-uniform stress state develops during the compression test, possibly due to compliance of the test frame. The data also indicates that the strain rate in the specimen is not constant, even though the crosshead speed of the hydraulic cylinder is.

The finite element method is used to simulate the non-ideal compression tests. The effective stiffness of the testing frame is included in the model, and a non-uniform axial displacement is gradually applied to the specimen as the test proceeds, keeping the average rate of displacement constant. Using the available experimental data as a reference, the current work aims to find the material model parameters, testing machine stiffness and displacement boundary conditions that best reproduce the experimental data by solving an inverse problem on virtually constructed experimental data. The material model chosen is the Mechanical Threshold Stress (MTS) model [1]. This model uses a state variable based work hardening law that is strain rate and temperature dependent.

1.1 The Mechanical Threshold Stress model

The mechanical threshold stress is defined as the material flow stress extrapolated to 0 K. The flow stress σ_y of a material is developed by scaling of the mechanical threshold to account for rate and temperature dependence [1]. The mechanical threshold, $\hat{\sigma}$, is separated into an athermal component $\hat{\sigma}_a$ and thermal components $\hat{\sigma}_t^\kappa$.

At different temperatures T and plastic strain rates $\dot{\varepsilon}$, the contributions to the flow stress σ_t^κ are related to their reference counterparts $\hat{\sigma}_t^\kappa$ through the scaling functions $S_t^\kappa(\dot{\varepsilon}, T)$, so that the flow stress

of a material, σ_y, is expressed as

$$\frac{\sigma_y}{\mu} = \frac{\hat{\sigma}_a}{\mu} + \sum_{\kappa} \frac{\sigma_t^{\kappa}}{\mu} = \frac{\hat{\sigma}_a}{\mu} + \sum_{\kappa} S_t^{\kappa}(\dot{\varepsilon}, T) \frac{\hat{\sigma}_t^{\kappa}}{\mu_o}. \tag{1}$$

μ_o is a reference value of the shear modulus μ, which is modeled by [2]

$$\mu = \tilde{\mu}(T) = \mu_o - \frac{D_o}{\exp\left(\frac{T_o}{T}\right) - 1}, \tag{2}$$

in which T_o and D_o are empirical constants. The temperature dependence of μ is included in the scaling functions S_t^{κ}. The material elastic modulus is also coupled to these constants by

$$E = 2\mu(1 + \nu), \tag{3}$$

where ν is chosen as 0.21 for this work.

In this work, an Arrhenius expression is used to describe interaction kinetics for short-range obstacles. A phenomenological relation is now used for the free energy function of stress [3]. In the standard MTS model, and the one used here, there are two thermal components, i.e. $\hat{\sigma}_t^{\kappa}$, $\kappa = 1, 2$. Using the notation $\hat{\sigma}_t^1 = \hat{\sigma}_i$ and $\hat{\sigma}_t^2 = \hat{\sigma}_{\varepsilon}$, Eq.(1) is written

$$\frac{\sigma_y}{\mu} = \frac{\hat{\sigma}_a}{\mu} + S_i(\dot{\varepsilon}, T) \frac{\hat{\sigma}_i}{\mu_o} + S_{\varepsilon}(\dot{\varepsilon}, T) \frac{\hat{\sigma}_{\varepsilon}}{\mu_o}, \tag{4}$$

where

$$S_i = \left[1 - \left(\frac{kT}{g_{oi}\mu b^3} \ln \frac{\dot{\varepsilon}_{oi}}{\dot{\varepsilon}}\right)^{1/q_i}\right]^{1/p_i} \quad \text{and} \quad S_{\varepsilon} = \left[1 - \left(\frac{kT}{g_{o\varepsilon}\mu b^3} \ln \frac{\dot{\varepsilon}_{o\varepsilon}}{\dot{\varepsilon}}\right)^{1/q_{\varepsilon}}\right]^{1/p_{\varepsilon}}. \tag{5}$$

The thermal portion of the yield stress (which does not evolve) is described by $\hat{\sigma}_i$ while $\hat{\sigma}_{\varepsilon}$ describes the interaction of mobile dislocations with the forest dislocation structure (which does evolve). In the scaling functions S_i and S_{ε}, k is the Boltzmann constant and b is the magnitude of the Burger's vector. g_{oi} and $g_{o\varepsilon}$ are the normalized activation energies for dislocations to overcome the obstacles; $\dot{\varepsilon}_{oi}$ and $\dot{\varepsilon}_{o\varepsilon}$ are constants while p and q are statistical constants that characterize the shape of the obstacle profiles ($0 \leq p_i, p_{\varepsilon} \leq 1$, $1 \leq q_i, q_{\varepsilon} \leq 2$) [3].

The evolution of $\hat{\sigma}_{\varepsilon}$ is given in rate form, by

$$\frac{d\hat{\sigma}_{\varepsilon}}{d\varepsilon} = \theta(T, \dot{\varepsilon}, \hat{\sigma}_{\varepsilon}) = \theta_o - \theta_r(T, \dot{\varepsilon}, \hat{\sigma}_{\varepsilon}), \tag{6}$$

where θ_o is the hardening due to dislocation accumulation (assumed constant) and θ_r is the dynamic recovery rate. The functional form of the hardening rate θ is chosen to fit experimental data. In this work it takes the tanh form [1, 4]

$$\theta = \theta_o \left(1 - \frac{\tanh\left[\frac{\alpha \hat{\sigma}_{\varepsilon}^s}{\hat{\sigma}_{\varepsilon s}}\right]}{\tanh(\alpha)}\right) \tag{7}$$

with $\alpha = 2$ [1]. $\hat{\sigma}_{\varepsilon s}$ is the saturation threshold stress while θ_o assumes the role of the initial hardening rate. The saturation threshold stress $\hat{\sigma}_{\varepsilon s}$ is a function of both strain rate and temperature, through the relation [4]

$$\ln \frac{\dot{\varepsilon}}{\dot{\varepsilon}_{\varepsilon so}} = \frac{g_{o\varepsilon s}\mu b^3}{kT} \ln \frac{\hat{\sigma}_{\varepsilon s}}{\hat{\sigma}_{\varepsilon so}} \tag{8}$$

where $\dot{\varepsilon}_{\varepsilon so}$, $g_{o\varepsilon s}$ and $\hat{\sigma}_{\varepsilon so}$ are empirically obtained constants.

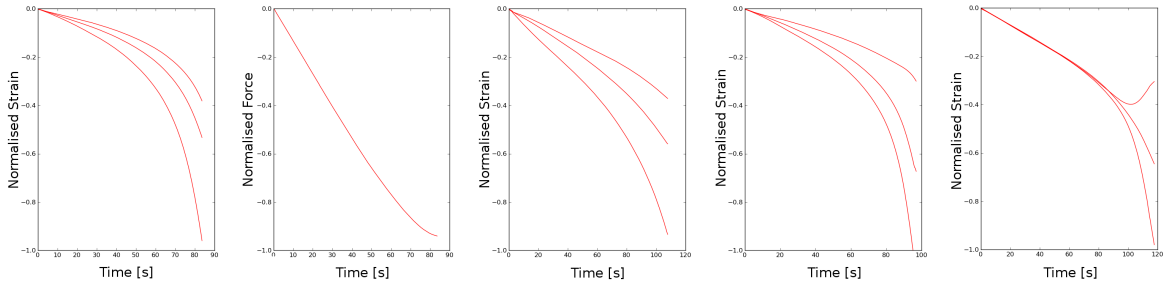

(a) (b) (c) (d) (e)

Figure 1: Normalised experimental strains and load cell data at room temperature. (a) Strains recorded by the strain gauges spaced evenly around the circumference of the test section with (b) the load cell data of the same experiment. (c), (d) and (e) Strain gauge measured strains of three other experiments.

1.2 Experimental Data

The experimental data is obtained from compression tests where 3 strain gauge readings are available at room temperature, along with hydraulic cylinder displacement and load cell data. The strain gauges are fixed to the centre of the experimental test specimen, 120° apart. Higher temperature data is also available at 150°C, 250°C, 350°C and 500°C. At these elevated temperatures however, only a single extensometer strain measurement is available.

The materials tested are used in high temperature and pressure applications. The specific application, exact material compound and grade is proprietary information and for this reason, figure axes and material parameter values are normalized in this report. A material test specimen similar to the one described by [5] is used for the experimental compression tests. This compression test specimen is essentially a modified version of a conventional cylindrical tensile specimen. The length of the test section is reduced in an attempt to avoid buckling and shear deformation modes during the compression test.

One of the demanding aspects of compression tests on these hard materials is the very high compressive strength and stiffness. The testing machine stiffness, which should ideally be orders of magnitude greater than that of the specimen, is inadequate in this case. Experimental data indicates that for a typical test the hydraulic cylinder displaces 1.4 mm, while the specimen test section only decreases height by about 0.4 mm. Elastic deformation of the testing machine frame seems to account for the remaining 1.0 mm displacement. From the strain gauge data of various room temperature compression tests seen in Figures 1(a), (c), (d) and (e) there appears to be some compressive instability, eccentric load condition or equivalent bending moment. Unfortunately, data for only a single extensometer is available for the elevated temperature tests. From all the room temperature data it seems plausible that the elevated temperature tests may also have experienced a similar non-ideal loading condition, but this cannot be taken into account due to the limited data.

The data suggests that there is no constant thermal stress component $\hat{\sigma}_i$. The constant thermal stress component of the mechanical threshold stress definition in Equation (4) therefore falls away. Neither k nor b are used anywhere other than the relationships ${}^{k}/_{g_{o\varepsilon}b^3}$ and ${}^{k}/_{g_{o\varepsilon s}b^3}$, so these two relationships are grouped into single variables. A list of the remaining MTS material parameters used as optimisation variables and constant parameters are given in Table 1.

In this work, the virtual experimental data is obtained by first conducting a finite element analysis. A varying displacement boundary condition is applied to the room temperature simulation so that a distribution of strain is recovered around the circumference of the test specimen centre. Two different displacement fields are used to set up two different virtual experiments at room temperature. These displacement fields produce strain distributions that have approximately the same order of magnitude difference at the end of the simulation as seen in the actual experimental data. Since the values of the material parameters used in the virtual experiment is known, an inverse analysis may be performed to determine the accuracy with which these known parameters and boundary conditions can be retrieved.

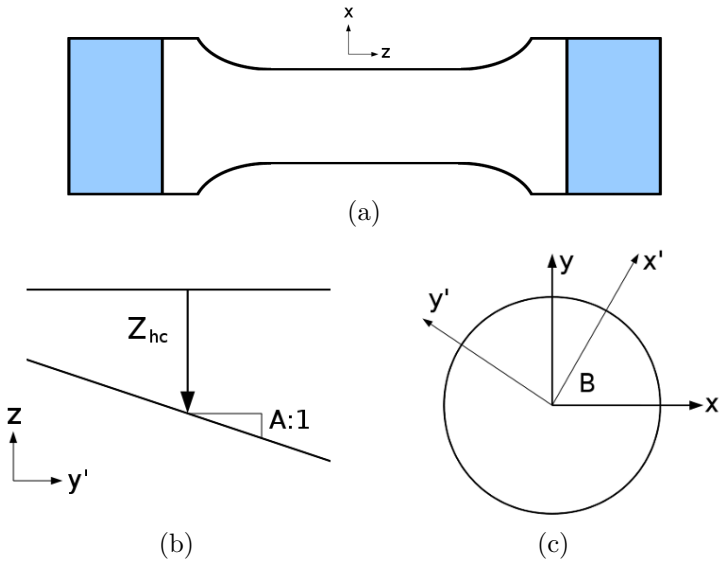

Figure 2: (a) Simple schematic illustrating the test section modelled with artificial material sections to accommodate the machine test frame stiffness. The two variables A and B that are used to describe the boundary displacement at a specific time are visible in (b) and (c).

2 Finite Element model

The central 35 mm of the test specimen is modelled with elastic properties as well as plastic behaviour using an MTS material model implemented into an Abaqus [6] user subroutine. 5 mm of artificial elastic material is added to the ends of the specimen. A representation of this can be seen in Figure 2(a). Hydraulic cylinder displacement can now be used as a boundary condition while the stiffness of the artificial material section can be changed during the inverse analysis procedure. By modelling it in this way, the experimental hydraulic cylinder displacement can be applied to the artificial material section. A correct choice of artificial material stiffness would then result in an effective strain rate and displacement experienced by the test specimen that best resembles the uniaxial conditions experienced during the actual test.

A spatially varying displacement field is applied to the artificial material section. If the uniaxial direction is chosen as the z-axis in the finite element analysis, a top face node n experiences a z-displacement of the form

$$z_n = A(t)\left(\sin(B)y_n + \cos(B)x_n\right) + Z_{hc}(t), \tag{9}$$

where t is the current fraction of time, $t \in [0, 1]$ and $Z_{hc}(t)$ is the hydraulic cylinder displacement as a function of this time fraction.

Table 1: List of MTS material parameters regarded as either fixed or optimisation variables for use in the inverse analysis.

Variables							
Parameter:	$\hat{\sigma}_a$	$\hat{\sigma}_{\varepsilon so}$	$k/g_{o\varepsilon}b^3$	$k/g_{o\varepsilon s}b^3$	θ_o	μ_o	D_o
Equation:	(1)	(8)	(5)	(8)	(7)	(2)	(2)
Constants and Initial Values							
Parameter:	$\hat{\sigma}_\varepsilon$	T_o	$\dot{\varepsilon}_{o\varepsilon}$	$\dot{\varepsilon}_{\varepsilon so}$	q_ε	p_ε	α
Equation:	(4)	(2)	(5)	(8)	(5)	(5)	(7)
Value:	0	200	10^6	10^6	1	$2/3$	2

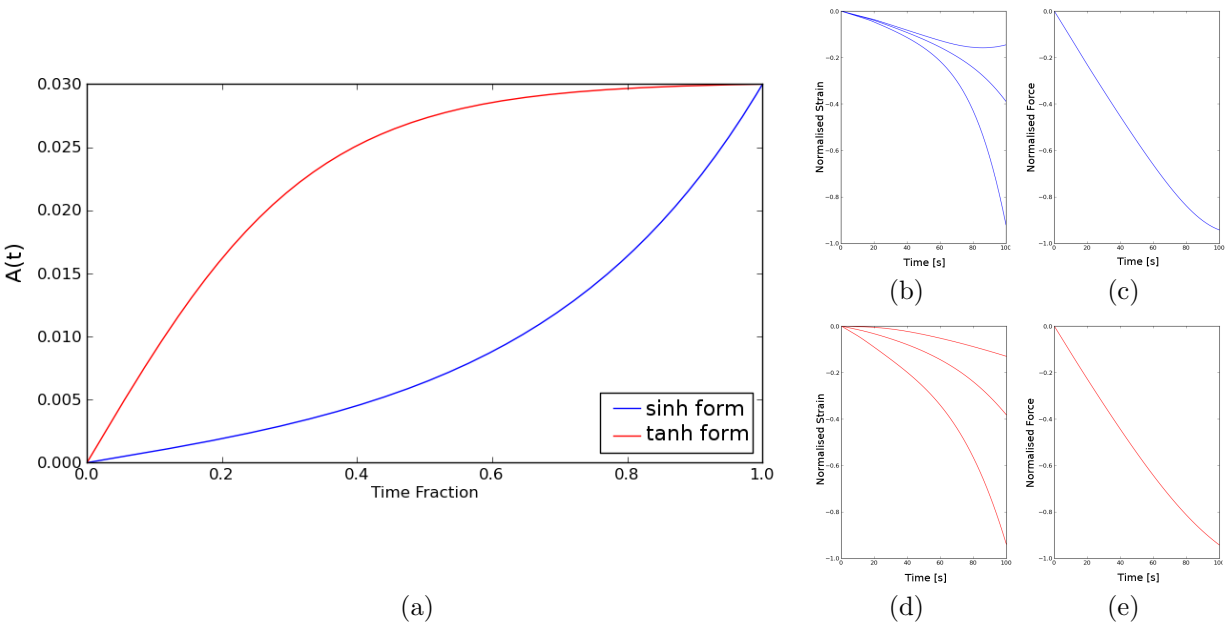

Figure 3: Curves selected to represent two possible forms of $A(t)$. These curves represent the definition of $A(t)$ in Equation (11), used for the displacement boundary conditions in the virtual experiments.

x_n and y_n are the x and y coordinates of node n with $A(t)$ and B two boundary properties illustrated in Figures 2(b) and (c). The displacement field variation $A(t)$ can also change as a function of the time fraction while it was decided that the angle (and so the neutral axis of the bending moment) would remain constant. Similarly, the z-displacement field at a bottom face node is determined by

$$z_n = -A(t)\left(\sin(B)y_n + \cos(B)x_n\right). \tag{10}$$

By modelling the top and bottom displacement fields in this way an equal and opposite equivalent bending moment can be approximated at a specific fraction of the total time.

2.1 Virtual Experiment Data

Two sets of virtual experimental data are obtained using the same MTS material parameters with a slightly different boundary condition on the room temperature virtual test. In both 25°C virtual experiments, the angle B is set to 4.5 radians while the virtual hydraulic cylinder displacement is chosen as $Z_{hc} = 1t$, $t \in [0, 1]$. The different experimental boundary conditions are obtained by different forms of $A(t)$. In the two virtual experiments, the form of $A(t)$ in Equations (9) and (10) is chosen as

$$A(t) = \frac{0.03 \times \tanh(3t)}{\tanh(3)} \quad \text{and} \quad A(t) = \frac{0.03 \times \sinh(3t)}{\sinh(3)}. \tag{11}$$

The curves that represent $A(t)$ as a function of the time fraction are visible in Figure 3(a). A 500°C virtual experiment is also set up. This high temperature virtual experiment was modelled as a perfect uniaxial compression test subject to a constant hydraulic cylinder displacement rate. The hydraulic cylinder displacement $Z_{hc} = 1t$, $t \in [0, 1]$ is again used with a different artificial material section stiffness. After the problems are solved using Abaqus, the following virtual data is extracted from each of the 25°C results:

- The logarithmic strain history of the central test section elements closest to the 0, $^2/_3\pi$ and $^4/_3\pi$ radian locations along the test section circumference. This virtual data is chosen to represent the three strain gauges' history in the original experiments.
- The total vertical reaction force on the top artificial material section. This is chosen to represent the experimental load cell data.

The normalised strain and force histories that result from the two forms of $A(t)$ can be seen in Figure 3(b) through (e). These histories are now used as virtual experimental data to test the idea of simultaneously estimating material parameters and boundary conditions by inverse analysis. A single set of high temperature FEA results is used to represent the high temperature experimental data. The total reaction force is again used to represent the load cell data while the average of the central test section element set logarithmic strain histories are used to represent the single extensometer data of the original experiment.

3 Inverse Analysis

To test the invertibility of this type of problem, the MTS material parameters are now determined by fitting force and strain curves to the 25°C and 500°C virtual experiment data. This inverse analysis aims to recover both the elastic as well as plastic behaviour of the material along with the artificial material stiffness at the different temperatures and boundary conditions, making it a fairly complex inverse parameter identification problem despite the seemingly simple geometry and setup.

Assuming no prior information is available on the shape of the displacement boundary condition that resulted from a chosen form of $A(t)$ in Equation (11), the invertibility of the problem is inspected using a piecewise linear approximation to $A(t)$. First, a single linear time variation is used to approximate the form of $A(t)$. Then a piecewise linear approximation using three and six intervals is inspected. The straight line approximation requires one unknown, while the three intervals and six intervals piecewise linear approximations require three and six unknowns respectively.

The optimisation is performed using the unconstrained optimisation algorithm `fmin`, available via the `scipy.optimize` [7] module in Python [8]. `fmin` is an implementation of the Nelder-Mead simplex algorithm. Although the `scipy.optimize` [7] module does give access to arguably better numerical optimisation algorithms, this is a very robust algorithm that only requires function value evaluations without additional gradient information from the user. Because of its robust nature, this algorithm was used in this initial work to first assess the invertibility of the problem.

3.1 Function Evaluation

Given a set of material and boundary condition parameters, a 25°C finite element job is constructed and solved using Abaqus [6]. The logarithmic strains at the same locations along the circumference of the central test section is extracted the same way as originally done to obtain virtual experiment data. These three strain histories are compared to the virtual experiment data. The total reaction force at the top surface of the inverse solution over time and that of the virtual experiment is compared. A finite element analysis for the 500°C problem is then constructed and also solved. The average logarithmic strains and total force histories are again extracted from the results as were done to initially obtain the virtual experimental data and compared to its corresponding virtual experiment data set. Each of the four strain histories and two force histories are compared by first normalising it so that the absolute maximum function value is unity. The function value returned is the sum of the mean squared error of the six normalised curve comparisons.

3.2 Results

The form of $A(t)$ is first approximated by a single linear time varying section. In this first approximation, the $A(t)$ approximation therefore only requires a single unknown. This unknown along with the angle B, artificial material stiffness at 25°C and 500°C as well as the seven MTS material parameters are estimated simultaneously. The form of $A(t)$ is then approximated by three piecewise linear time varying sections that requires an additional two unknowns.

The single line and three piecewise approximation runs were given the same initial guess for all of the corresponding parameters. The two additional parameters in the three interval piecewise linear approximation were also chosen in such a way that the initial approximation was still a straight line. In contrast, the six interval piecewise linear approximation run was continued from the three interval result, taking the parameter values at the termination of the three piece result and adding three additional

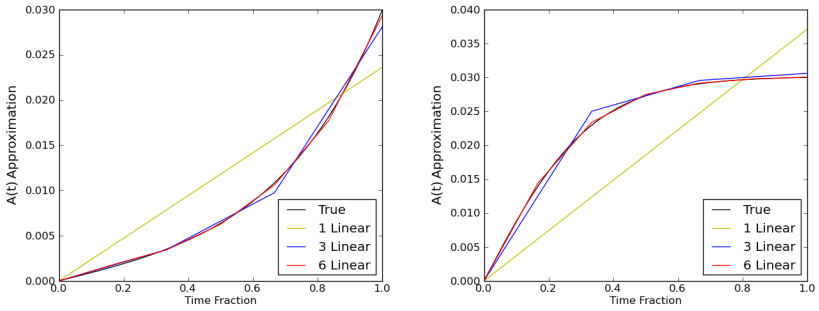

(a) (b)

Figure 4: The two forms of $A(t)$, used in the virtual experiment displacement boundary condition compared to the optimum approximations found by using either a single line, three or six piecewise linear approximation. (a) The sinh and (b) tanh virtual experiment results.

points on the curve that approximates $A(t)$. Inverse analysis using this single linear approximation, three interval piecewise linear and continued six interval piecewise linear approximation to the form of $A(t)$ is performed on both the sinh and tanh boundary condition virtual experiments.

The results of the final approximation to the form of $A(t)$ in the boundary displacement description using a single, three and six interval piecewise linear approximation are presented in Figure 4. The normalised parameter results at the end of each optimisation run are presented in Table 2. Figure 5 shows the curves that result from the analysis using the initial parameters while Figures 6 through 8 show the inverse analysis results.

Table 2: Normalised parameter identification results and details of the inverse analyses performed on the sinh and tanh virtual experiments.

	Sinh BC Virtual Experiment Piecewise Linear Approximation			Tanh BC Virtual Experiment Piecewise Linear Approximation		
	1 Linear	3 Linear	6 Linear	1 Linear	3 Linear	6 Linear
Variables:	11	13	16	11	13	16
Iteration:	2,200	2'601	+ 2'444	1'395	2'602	+ 1'356
F Value						
Initial:	3.504×10^{-2}	3.504×10^{-2}	1.776×10^{-4}	8.321×10^{-2}	8.321×10^{-2}	2.017×10^{-4}
Final:	3.936×10^{-3}	1.776×10^{-4}	1.346×10^{-5}	9.121×10^{-3}	2.017×10^{-4}	5.107×10^{-6}
Parameter						
E_{298K} *	1.03226	0.99988	1.00019	0.95957	0.99953	0.99997
E_{773K} *	1.00581	1.00026	1.00200	0.93575	0.99155	0.99993
μ_o *	0.78729	0.99029	0.99992	1.98992	1.06192	0.99770
D_o *	0.45060	0.97611	1.01220	1.54866	0.72243	0.99628
$\hat{\sigma}_a$ *	0.02085	0.97637	0.98440	1.18953	0.29522	1.01126
$\hat{\sigma}_{\varepsilon so}$ *	1.15135	0.99636	0.99641	1.27623	1.15835	0.99869
θ_o *	2.85187	1.04099	1.02566	0.29879	1.22473	0.99488
$k/g_{o\varepsilon}b^3$ *	0.25332	1.10369	1.04966	0.30701	0.83581	0.95063
$k/g_{o\varepsilon s}b^3$ *	3.22614	0.96475	1.10172	0.17437	0.52390	0.99750

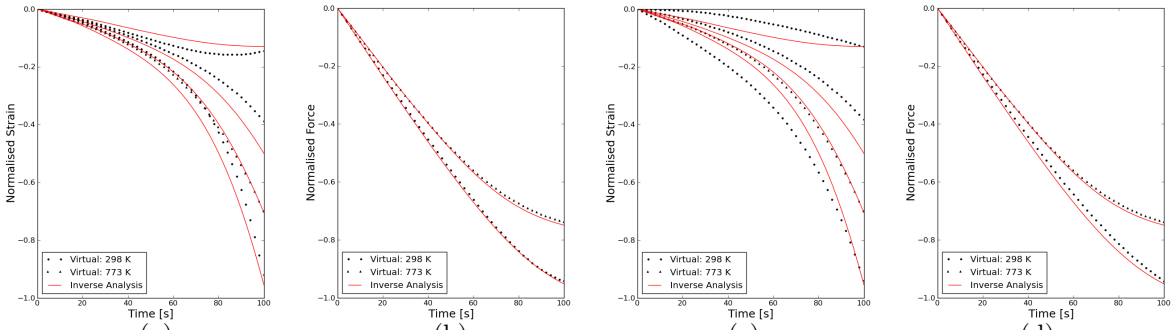

(a) (b) (c) (d)

Figure 5: Initial fit on the sinh and tanh virtual experimental data. (a) The strain history and (b) force history fit on the sinh virtual experiment. (c) The strain history and (d) force history fit on the tanh virtual experiment.

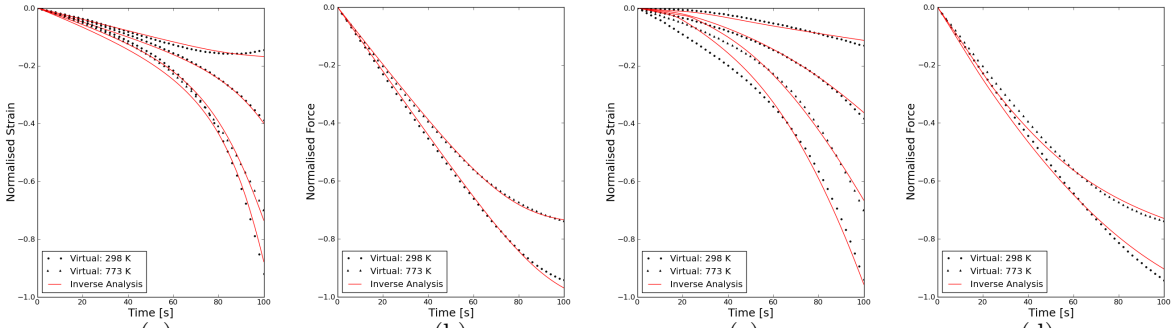

(a) (b) (c) (d)

Figure 6: Resulting optimum fit determined by inverse analysis on the sinh and tanh virtual experimental data using a linear approximation of $A(t)$. (a) The strain history and (b) force history fit on the sinh virtual experiment. (c) The strain history and (d) force history fit on the tanh virtual experiment.

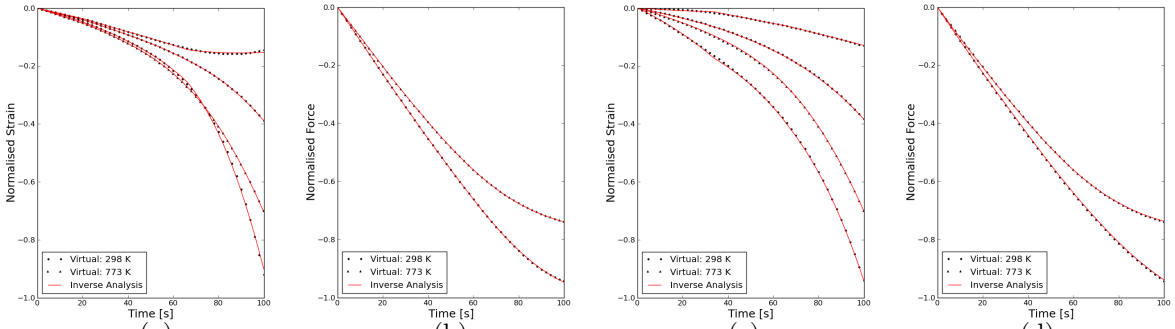

(a) (b) (c) (d)

Figure 7: Resulting optimum fit determined by inverse analysis on the sinh and tanh virtual experimental data using a three piecewise linear approximation of $A(t)$. (a) The strain history and (b) force history fit on the sinh virtual experiment. (c) The strain history and (d) force history fit on the tanh virtual experiment.

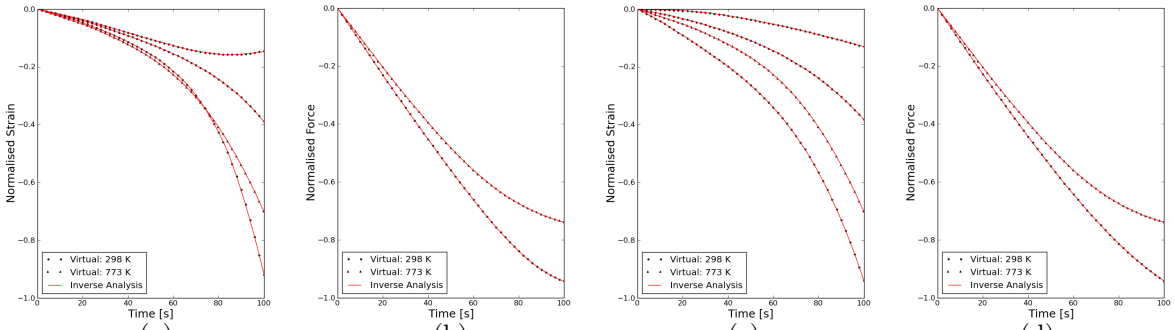

Figure 8: Resulting optimum fit determined by inverse analysis on the sinh and tanh virtual experimental data using a six piecewise linear approximation of $A(t)$. (a) The strain history and (b) force history fit on the sinh virtual experiment. (c) The strain history and (d) force history fit on the tanh virtual experiment.

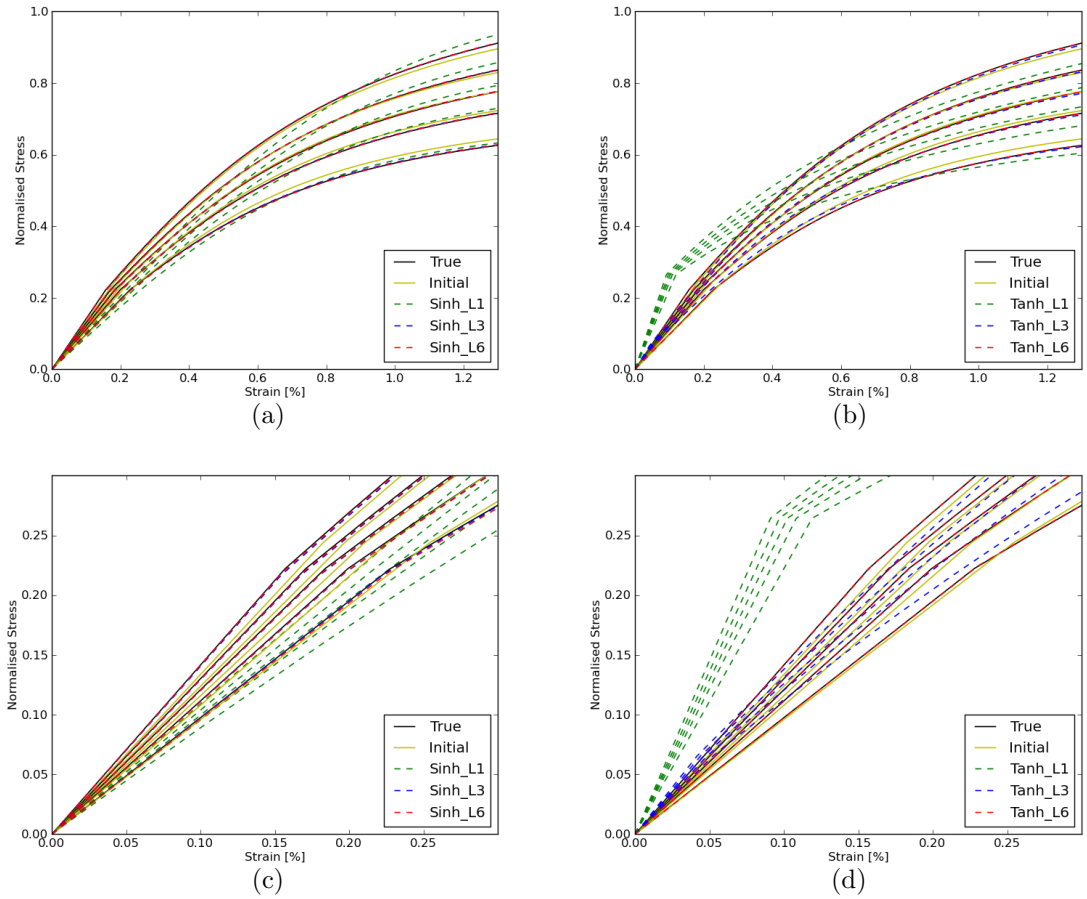

Figure 9: The MTS material response at 25°C, 150°C, 250°C, 350°C and 500°C for a constant strain rate of 0.0001 s^{-1}. (a) The various materials approximated using the sinh form of $A(t)$ virtual experiment with detail of the initial yield stress in (c). (b) The various materials approximated using the tanh form of $A(t)$ virtual experiment with detail of the initial yield stress in (d). The approximated material responses are plotted over the response of the actual material with known property values in black.

In Table 2 and Figure 6, it is visible that using too simple an approximation on the boundary condition could result in an inadequate fit and material parameters that are far from the desired accuracy. Here it seems that the material parameters are exploited to compensate for the inadequate capture of the boundary condition. This is also visible in the fit between the green dashed lines and the true material response in Figures 9(a) through (d).

Not surprisingly, the higher the resolution used to approximate the form of $A(t)$ in the boundary description, the better the ability to capture the true form and the material parameters. In Table 2 and Figure 9 it is also visible that an overall improvement on the accuracy of the material parameter identification is achieved when the inverse analysis has the ability to better capture the true boundary condition. Good correspondence is visible between the true material response (black lines) and that determined at the end of the six interval piecewise linear approximation (red dashed lines) in Figure 9.

4 Conclusions

In this initial work it would seem that the inverse problem does not present major issues in simultaneously determining the material properties and test conditions. Although the actual form of the displacement boundary condition that would best replicate the experimental data is unknown, it has been demonstrated that a piecewise linear approximation can produce sufficient accuracy.

Ideally, a very fine boundary condition parameterisation should be utilised during the identification of material parameters on real experimental data. This however introduces additional unknowns and could make the optimisation a very expensive and time consuming procedure. Although this initial study into the invertibility of the problem seems promising, additional investigation into better optimisation algorithms and alternative inverse problem formulations could reduce the time required and allow for the capture of material properties with increased accuracy.

5 References

[**1**] Follansbee P S and Kocks U F, A Constitutive Description of Copper Based on the Use of the Mechanical Threshold Stress as an Internal State Variable. *Acta Metall 36*, 1988, 81-93.

[**2**] Varshni Y P, Temperature Dependence of the Elastic Constants. *Phys Rev B 2*, 1970, 3952-3958.

[**3**] Kocks U F, Argon A S and Ashby M F, Thermodynamics and Kinetics of Slip. *In: Progress in Materials Science 19: Pergamon Press*, 1975, New York.

[**4**] Chen S R and Gray G T, Constitutive Behaviour of Tantalum and Tantalum-Tungsten Alloys. *Metall and Mat Trans 27(A)*, 1996, 2994-3006.

[**5**] Dunlay W A, Tracy C A and Perrone P J, A Proposed Uniaxial Compression Test for High Strength Ceramics. *Report: U.S. Army Materials Technology Laboratory MTL-TR-89-89*, 1989.

[**6**] Abaqus FEA software, SIMULIA web site. Dassault Systèmes.
`URL = http://www.3ds.com/products/simulia/portfolio/`

[**7**] SciPy: Scientific Tools for Python. `URL = www.scipy.org`

[**8**] Python programming language. `URL = www.python.org`